Astronomy & Astrophysics

Who is eating the outflow? High-angular resolution study of an intermediate-mass protostar in L1206

M. T. Beltrán[1], J. M. Girart[2], and R. Estalella[1]

[1] Departament d'Astronomia i Meteorologia, Universitat de Barcelona, Av. Diagonal 647, 08028 Barcelona, Catalunya, Spain
e-mail: mbeltran@am.ub.es
[2] Institut de Ciències de l'Espai (CSIC-IEEC), Campus UAB, Facultat de Ciències, Torre C-5, 08193, Bellaterra, Catalunya, Spain

ABSTRACT

Context. Up to now only a few intermediate-mass molecular outflows have been studied with enough high-angular resolution.
Aims. The aim of this work is to study in detail the intermediate-mass YSO IRAS 22272+6358A, which is embedded in L1206, and its molecular outflow, to investigate the interaction of the outflow with the dense protostellar material and to compare their properties with those of lower mass counterparts.
Methods. We carried out OVRO observations of the 2.7 mm continuum emission, CO ($J = 1 \rightarrow 0$), $C^{18}O(J = 1 \rightarrow 0)$, and HC_3N ($J = 12 \rightarrow 11$) to map the core of L1206 with high-angular resolution and to derive the properties of the dust emission, the molecular outflow, and the dense protostellar envelope.
Results. The 2.7 mm continuum emission has been resolved into four sources, labeled OVRO 1, 2, 3, and 4. The intermediate-mass Class 0/I object OVRO 2, with a mass traced by the dust emission of 14.2 $M_\odot$, is the source associated with IRAS 22272+6358A. The CO ($J = 1 \rightarrow 0$) observations have revealed a very collimated outflow driven by OVRO 2, at a PA $\simeq 140°$, that has a very weak southeastern red lobe and a much stronger northwestern blue lobe. Photodissociation toward the red lobe produced by the ionization front coming from the bright-rimmed diffuse HII region could be responsible for the morphology of the outflow. The spatial correlation between the outflow and the elongated dense protostellar material traced by HC_3N ($J = 12 \rightarrow 11$) suggests an interaction between the molecular outflow and the protostellar envelope. Shocks produced by the molecular outflow, and possibly by the shock front preceding the ionization front, could account for the southern enhancement of HC_3N. The properties of the intermediate-mass protostar OVRO 2 and the molecular outflow are consistent with those of lower mass counterparts. The $C^{18}O$ abundance relative to molecular hydrogen estimated toward OVRO 2 is 3×10^{-8}, a value ∼6 to 13 times lower than typical abundances estimated toward molecular clouds. The most plausible explanation for such a difference is CO depletion toward OVRO 2.

Key words. ISM: individual objects: L1206 – ISM: individual objects: IRAS 22272+6358A – ISM: jets and outflows – stars: circumstellar matter – stars: formation

1. Introduction

Molecular outflows are a ubiquitous phenomenon during the earliest stages of star formation for Young Stellar Objects (YSOs) of all masses and luminosities. During the last decades, many studies have been devoted to the study and description of the physical properties of molecular outflows driven by low-mass protostars and of their embedded driving sources (e.g., Bachiller 1996; Richer et al. 2000). In recent years, high-mass molecular outflows have also been studied in detail, and many surveys have been carried out toward massive star-forming regions to achieve a more accurate picture of their morphology and properties (e.g., Shepherd & Churchwell 1996a,b; Zhang et al 2001; Shepherd 2005). However, although the interest for the lower and, in particular, for the higher end of the mass spectrum has been growing in recent years, this has not been the case for intermediate-mass protostars, with masses in the range $2\,M_\odot \leq M_\star \leq 10\,M_\odot$, which power energetic molecular outflows. In fact, only few deeply embedded intermediate-mass protostars are known to date, and only a very limited number of their outflows have been studied at high-angular resolution (e.g., NGC 7129: Fuente et al. 2001; HH288: Gueth et al. 2001; IRAS 21391+5802: Beltrán et al. 2002).

Intermediate-mass protostars are rare in comparison to their low-mass counterparts and tend to be located at greater distances. The immediate vicinity of intermediate-mass protostars is a very complex environment, where the extended emission is usually resolved into more than one source when observed at high-angular resolution (e.g., G173.58+2.45: Shepherd & Watson 2002; IRAS 21391+5802: Beltrán et al. 2002). The molecular outflows driven by intermediate-mass objects are usually more energetic. Thus, their interaction with the circumstellar gas and dust material surrounding the protostars is expected to be stronger and more dramatic, disrupting the envelopes and pushing away the dense gas at high velocities. Although these outflows are, in general, less collimated and more chaotic than those of low-mass stars (e.g., NGC 7129: Fuente et al. 2001), this could probably be due to observational constraints. Since these regions are located, on average, further away, these outflows are usually observed with less linear spatial resolution than nearby low-mass flows. However, when observed with high-angular resolution, their appearance seems to be more collimated and less chaotic (e.g., HH 288: Gueth et al. 2001; IRAS 21391+5802: Beltrán et al. 2002). Therefore, to better understand intermediate-mass stars and compare their morphology and evolution with those of low-mass stars, more high-angular observations of the dust and gas around them are needed.

**Table 1.** Parameters of the OVRO observations.

Observation	Configuration	Frequency (GHz)	Synthesized beam		Bandwidth (MHz)	Spectral resolution (km s^{-1})	rms noise[a] (mJy beam^{-1})
			HPBW (arcsec)	PA (deg)			
2.7 mm continuum	L, C	112.53	6.3×4.8	−27	4000	−	1.4
CO ($J = 1 \rightarrow 0$)	L, C	115.27	8.0×6.3	−29	22.5	0.65	45
C^{18}O ($J = 1 \rightarrow 0$)	L, C	109.78	8.0×6.6	−32	7.5	0.68	40
HC$_3$N ($J = 12 \rightarrow 11$)	L, C	109.17	8.1×6.7	−37	7.5	0.69	40

[a] For the molecular line observations the 1σ noise is per channel.

In this paper, we present a detailed interferometric study of the intermediate-mass protostar IRAS 22272+6358A and of its molecular outflow. IRAS 22272+6358A is a 1200 $L_\odot$ (Sugitani et al. 1989) YSO located at a distance of 910 pc (Crampton & Fisher 1974) and deeply embedded in the bright-rimmed cloud L1206 (BRC 44: Sugitani et al. 1991). This infrared source has no optical counterpart, and at near-infrared wavelengths, the embedded source has only been seen in scattered light (Ressler & Shure 1991). At far-infrared wavelengths, the source, undetected at 12 μm, emits most of its energy at 60 and 100 μm and has a flux density at 100 μm greater than that at 60 μm. This means that its $T(60/100)$ color temperature is lower than 50 K (38 K; Casoli et al. 1986), and therefore, that the source is very embedded, cold, and young. The embedded source has been detected at 2.7 and 2 mm (Wilking et al. 1989; Sugitani et al. 2000), but not at 2 or 6 cm wavelengths (Wilking et al. 1989; McCutcheon et al. 1991). Sugitani et al. (1989) have discovered a CO molecular outflow in the region, although they have only mapped the blueshifted outflow lobe, since the redshifted lobe was too faint to be mapped with the sensitivity achieved with their CO ($J = 1 \rightarrow 0$) 4-m radio telescope observations. The core toward IRAS 22272+6358A has also been observed in different high-density tracers, such as HCO$^+$ (Richards et al. 1987), NH$_3$ (Molinari et al.1996), CS and N$_2$H$^+$ (Williams & Myers 1999), and ^{13}CO and C^{18}O (Ridge et al. 2003).

2. Observations

Millimeter interferometric observations of L1206 at 2.7 mm were carried out with the Owens Valley Radio Observatory (OVRO) Millimeter Array of six 10.4 m telescopes in the L (Low) and C (Compact) configurations, on May 1 and June 1, 2003, respectively. The data taken in both array configurations were combined, resulting in baselines ranging from 15 to 115 m, which provided sensitivity to spatial structures from about 4″.8 to 37″. The digital correlator was configured to simultaneously observe the continuum emission and some molecular lines. Details of the observations are given in Table 1. The phase center was located at α(J2000) = 22^{h}28^{h}51^s.50, δ(J2000) = +64°13′42″.3. Bandpass calibration was achieved by observing the quasars 3C84, 3C273, and 3C345. Amplitude and phase were calibrated by observations of the nearby quasar J1927+739, whose flux density was determined relative to Uranus. The uncertainty in the amplitude calibration is estimated to be ~20%. The OVRO primary beam is ~64″ (*FWHM*) at 115.27 GHz. The data were calibrated using the MMA package developed for OVRO (Scoville et al. 1993). Reduction and analysis of the data were carried out using standard procedures in the MIRIAD and GILDAS software packages. We subtracted the continuum from the line emission directly in the (*u, v*) domain for C^{18}O ($J = 1 \rightarrow 0$) and HC$_3$N ($J = 12 \rightarrow 11$), and in the image domain for CO ($J = 1 \rightarrow 0$).
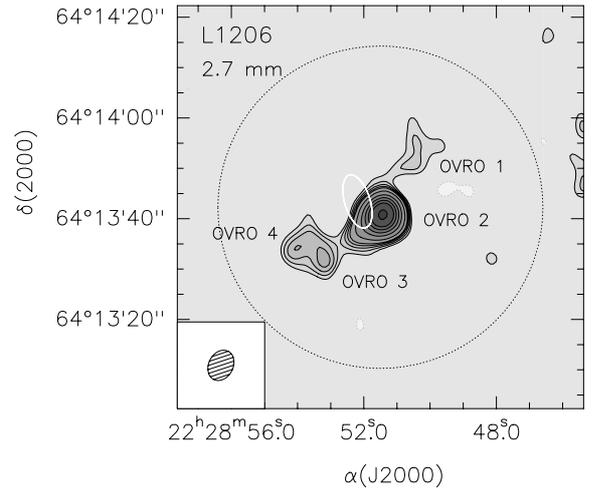
Fig. 1. OVRO map of the 2.7 mm continuum emission toward the core of L1206. The synthesized beam is 6″.3 × 4″.8 at PA = −27° and is drawn in the bottom left corner. The rms noise of the map, σ, is 1.4 mJy beam^{-1}. The contour levels are −5σ, −3σ, 3 to 7 times σ by 1σ, 10σ, 15 to 30 times σ by 5σ, and 40σ. The error ellipse of IRAS 22272+6358A is indicated in white. The dotted circle represents the OVRO primary beam (50% attenuation level).

3. Results

3.1. Dust emission

In Fig. 1 we show the OVRO map of the 2.7 mm continuum emission toward the core of L1206, where IRAS 22272+6358A is embedded. The continuum dust emission mapped at 2 mm by Sugitani et al. (2000) is resolved out in four different clumps, labeled OVRO 1, OVRO 2, OVRO 3, and OVRO 4, with the higher angular resolution of our interferometric observations. The position, the flux density at 2.7 mm, the deconvolved size of the sources (measured as the geometrical mean of the major and minor axis of the half-peak intensity contour around each source), the mass of the gas for each source, and the average H$_2$ volume and column density are given in Table 2. The total integrated flux at 2.7mm is ~120 ± 24 mJy. This value is consistent with the 2.7 mm expected flux of ~125 mJy derived from the 2 mm integrated flux of 414 mJy obtained with the single dish Nobeyama 45-m telescope (Sugitani et al. 2000) for a dust absorption coefficient proportional to ν^2. Therefore, this indicates that no significant fraction of the total flux has been filtered out by the interferometer.

The strongest source detected at 2.7 mm in the region is OVRO 2. As can be seen in Fig. 1, this source is the object associated with the infrared source IRAS 22272+6358A. OVRO 2 is located at the center of the CO molecular outflow detected in the region (see the next section and Fig. 2), which suggests that it is its driving source. The millimeter emission of OVRO 2 shows

Table 2. Positions, millimeter flux densities, sizes, and masses of the cores detected in L1206.

Core	Position α(J2000) h m s	Position δ(J2000) $\circ$ $'$ $''$	I_ν^{peak}(2.7mm)^a (mJy beam^{-1})	S_ν(2.7mm)^b (mJy)	θ^c (arcsec)	Mass^d ($M_\odot$)	n(H$_2$)^e (cm^{-3})	N(H$_2$)^e (cm^{-2})
OVRO 1	22 28 50.49	+64 13 50.7	6.8 ± 1.4	9.8 ± 2.0	9.3	1.6	6.5×10^5	5.5×10^{22}
OVRO 2^f	22 28 51.41	+64 13 41.1	59.2 ± 11.8	86.0 ± 17.2	3.5	14.2	1.1×10^8	3.4×10^{24}
OVRO 3	22 28 53.25	+64 13 32.1	10.9 ± 2.2	11.0 ± 2.2	5.4	1.8	3.7×10^6	1.8×10^{23}
OVRO 4	22 28 53.98	+64 13 34.5	10.7 ± 2.1	13.0 ± 2.6	5.6	2.2	4.0×10^6	2.0×10^{23}

^{a} Peak intensity corrected for primary beam response. The uncertainty in the values of the flux density is ~20%.

^{b} Integrated flux density corrected for primary beam response. The uncertainty in the values of the flux density is ~20%.

^{c} Deconvolved geometrical mean of the major and minor axes of the half-peak intensity contour.

^{d} Total (gas+dust) circumstellar mass, obtained assuming a dust temperature of 33 K (see Sect. 4.1).

^{e} Average H$_2$ volume and column density estimated assuming spherical symmetry and a mean molecular mass per H$_2$ molecule of $2.8m_{\text{H}}$.

^{f} Associated with IRAS 22272+6358A.
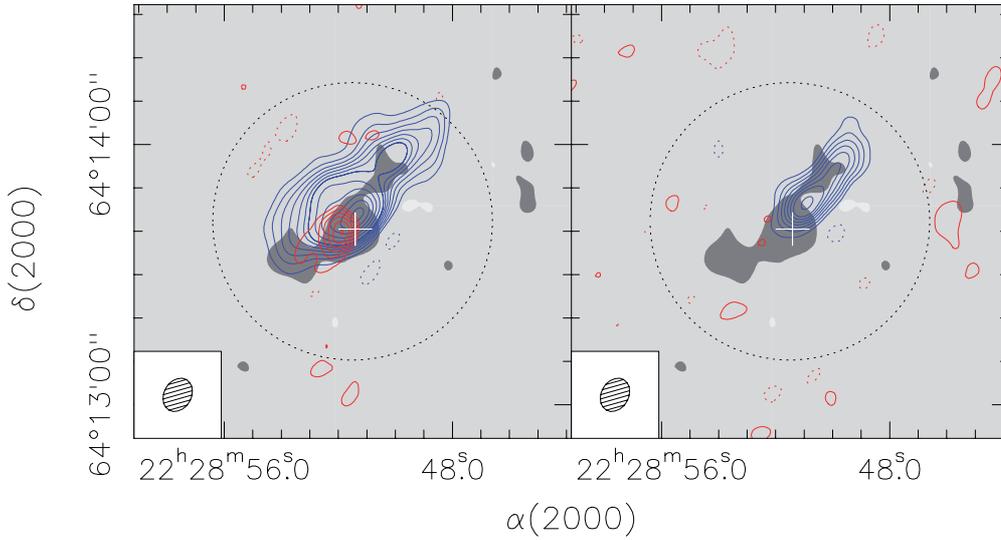
Fig. 2. CO ($J = 1 \rightarrow 0$) emission integrated in different velocity intervals, (-19.5, -13.5) km s^{-1} for the low-velocity blueshifted emission (*left panel; blue contours*), (-8.5, -2.5) km s^{-1} for the redshifted one (*left panel; red contours*), (-30.5, -19.5) km s^{-1} for the high-velocity blueshifted emission (*right panel; blue contours*), and (-2.5, $+8.5$) km s^{-1} for the high-velocity redshifted one (*right panel; red contours*), overlaid on the 2.7 mm continuum emission (*greyscale*). Contour levels are -3σ, 3 to 15 times σ by steps of 2σ, and 15 to 35 times σ by steps of 4σ, where 1σ is 0.5 Jy beam^{-1} km s^{-1} (*left panel; blue contours*), 0.18 Jy beam^{-1} km s^{-1} (*left panel; red contours*), 0.4 Jy beam^{-1} km s^{-1} (*right panel; blue contours*), and 0.15 Jy beam^{-1} km s^{-1} (*right panel; red contours*). The synthesized beam is drawn in the bottom left corner. The dotted circle represents the OVRO primary beam (50% attenuation level). The white cross marks the millimeter continuum position of OVRO 2.

two components, a centrally peaked source, which has a diameter of ~3″5 (~3200 AU) at the half-peak intensity contour of the dust emission, plus an extended and quite spherical envelope, which has a size of ~13″ (~11 800 AU) at the 3σ contour level. By fitting an elliptical Gaussian to the visibility data at the position of the dust emission peak, we found a total flux of 78 mJy and a size of 3″6 ± 0″3 × 2″6 ± 0″2 at PA = $-75°$. This size corresponds to a linear size of ~3200 × 2400 AU. These sizes are consistent with the values found for envelopes around low- and intermediate-mass protostars (e.g., Hogerheijde et al 1997, 1999; Looney et al. 2000; Fuente et al. 2001; Beltrán et al. 2002).

The source OVRO 1 is a clump, located ~11″ northwest of OVRO 2, elongated along the CO outflow axis (see Fig. 2). In fact, as can be seen in this figure, OVRO 1 clearly coincides with the blueshifted emission lobe, and therefore, it could be dusty material entrained by the outflow. The other two sources in L1206, OVRO 3 and 4, which are located ~15–18″ southeast of OVRO 2, have similar flux densities (~11–13 mJy) and deconvolved sizes (~5000 AU). Both sources are separated by only ~5″3 (~5000 AU) and could share a common envelope.

3.2. The molecular outflow: CO emission

The molecular outflow in L1206 associated with IRAS 22272+6358A, that is, OVRO 2, has been previously studied through lower angular resolution CO observations by Sugitani et al. (1989). However, since the red wing of this outflow is so weak, those authors were not able to map the red lobe. In addition, from their CO blueshifted emission integrated map, the direction of the outflow is not clear . The observations reported in this study significantly improve the angular resolution of the outflow maps, revealing the structure of the molecular outflow in detail, as well as its direction. In addition, we have been able to detect and map the weak outflow redshifted emission.

Figure 2 shows the maps of the integrated CO ($J = 1 \rightarrow 0$) emission in two different blueshifted and redshifted velocity intervals. The systemic velocity, V_{LSR}, reported in the literature is roughly -10 km s^{-1} (Richards 1987; Sugitani et al. 1989; Wilking et al. 1989; Wouterloot & Brand 1989; Williams & Myers 1999). However, from our fits to the C^{18}O ($J = 1 \rightarrow 0$) and HC$_3$N ($J = 12 \rightarrow 11$) spectra, we have estimated a systemic
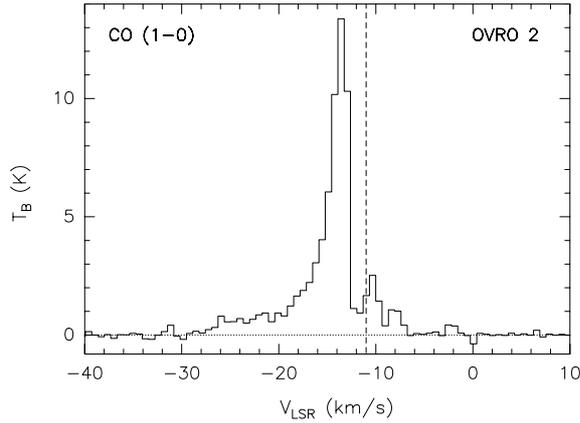
Fig. 3. CO ($J = 1 \rightarrow 0$) spectrum obtained at the position of OVRO 2 in L1206. The continuum has been subtracted. The 1σ level in one channel is 0.10 K. The conversion factor is 1.82 K/Jy beam^{-1}. The dashed vertical line indicates the systemic velocity of -11 km s^{-1}.

velocity $V_{\text{LSR}} \simeq -11$ km s^{-1} (see the next sections), which is the value used in this paper. Regarding the line widths in the region, which have been estimated from CO and CS and isotopomers, HCO$^+$, and N$_2$H$^+$ lines, the values derived are in the range 0.7 to 3.0 km s^{-1} (Richards 1987; Wilking et al. 1989; Wouterloot & Brand 1989; Molinari et al. 1996; Williams & Myers 1999; Ridge et al. 2003). Therefore, taking this into account, we conservatively considered the CO ambient cloud velocity interval to be $(-13.5, -8.5)$ km s^{-1}, that is, -11 ± 2.5 km s^{-1}. For the outflow, we took the $(-19.5, -13.5)$ km s^{-1} velocity interval for the low-velocity blueshifted emission, $(-8.5, -2.5)$ km s^{-1} for the redshifted one, $(-30.5, -19.5)$ km s^{-1} for the high-velocity blueshifted emission, and $(-2.5, +8.5)$ km s^{-1} for the redshifted one. As can be seen in Fig. 2, the molecular outflow is elongated in the direction of PA = 140° and has a very weak redshifted emission. In fact, the southeastern red lobe is only visible at low outflow velocities. The outflow is clearly centered at the position of OVRO 2, which seems to be its driving source. Figure 3 shows the CO ($J = 1 \rightarrow 0$) spectrum toward the position of OVRO 2, where a blueshifted wing that extends to very high velocities and a weak redshifted wing are clearly visible. In this figure, a strong self-absorption observed for the central velocity channels is also visible. This self-absorption feature is probably due to the filtering out of part of the extended emission by the interferometer, although we cannot exclude opacity effects as well, and this makes it impossible to study the cloud structure with CO ($J = 1 \rightarrow 0$). The direction of the outflow and the presence of a red wing are also confirmed by the position-velocity (PV) cut done along the major axis of the outflow (PA = 140°) and centered in the projection of the OVRO 2 dust emission peak position onto the outflow axis (Fig. 4).

This picture of the molecular outflow supports the scenario drawn by Ressler & Shure (1991) from near-infrared polarimetry, photometry, and imaging of the core of L1206. According to these authors, the near-infrared northwestern object named A-1, which is composed of scattered light, is the blueshifted lobe of the jet pointed slightly toward us, while the weaker southeastern object A-2, also composed of scattered light, is the redshifted lobe pointed away. The position of these two lobes coincides with the CO blueshifted and redshifted lobes, respectively. The protostar that is powering the outflow has to be heavily embedded, as is not detected at near-infrared wavelengths. Ressler & Shure (1991) propose that the driving source is a
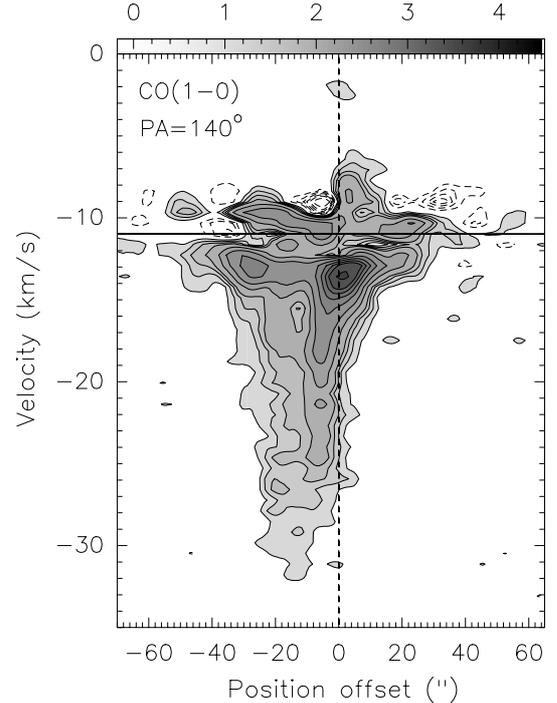

Fig. 4. PV plot of the CO ($J = 1 \rightarrow 0$) emission along the major axis, PA = 140°, of the molecular outflow. The position offset is relative to the projection of the 2.7 mm continuum emission peak onto the outflow axis, α(J2000) = 22$^{\text{h}}$28$^{\text{h}}$51$^{\text{s}}$52, δ(J2000) = +64°13′41″.7. Contours are -1.2, -0.9, -0.72, -0.54, -0.36, -0.18, 0.18, 0.36, 0.54, 0.72, 0.90, 1.2, 1.8, 2.7, 3.6, 4.5, 5.4, and 7.2 Jy beam^{-1}. The horizontal line marks the systemic velocity, $V_{\text{LSR}} = -11$ km s^{-1}.

Class I object with an optically thick disk lying almost edge-on to the line-of-sight, and located at α(J2000) = 22$^{\text{h}}$28$^{\text{h}}$51$^{\text{s}}$54, δ(J2000) = +64°13′42″.3, which is roughly coincident with the 2.7 mm OVRO 2 position (see Table 2).

3.3. C^{18}O emission

Figure 5 shows the velocity channel maps for the C^{18}O ($J = 1 \rightarrow 0$) emission around the systemic velocity, $V_{\text{LSR}} \simeq -11$ km s^{-1}, overlaid on the continuum emission. The emission integrated over the central channels, velocity interval $(-12.4, -8.3)$ km s^{-1}, is shown in the top panel of Fig. 6. The emission is dominated by a central compact component that peaks at the position of the continuum intermediate-mass continuum source OVRO 2, as can be clearly seen for the channel maps at velocities of -11.7 and -12.4 km s^{-1} (see Fig. 5). Therefore, such emission traces the innermost part of the protostellar envelope. For velocities between -9.7 and -11.0 km s^{-1}, the C^{18}O emission shows an additional extended component elongated north and east of OVRO 2, and also in part associated with the continuum sources OVRO 3 and 4. As can be seen in the channel and integrated maps, there is also some redshifted emission, visible at velocities of -8.3 and -9.0 km s^{-1}, which is located in the same direction as the CO redshifted lobe (see Fig. 2), but much more southeastwards than the emission traced by CO. The total integrated intensity of the central emission is ~15 Jy beam^{-1} km s^{-1} and has a deconvolved size, measured as the geometrical mean of the major and minor axes of the half-peak intensity contour of the gas, of 11″.4 or ~10 400 AU.
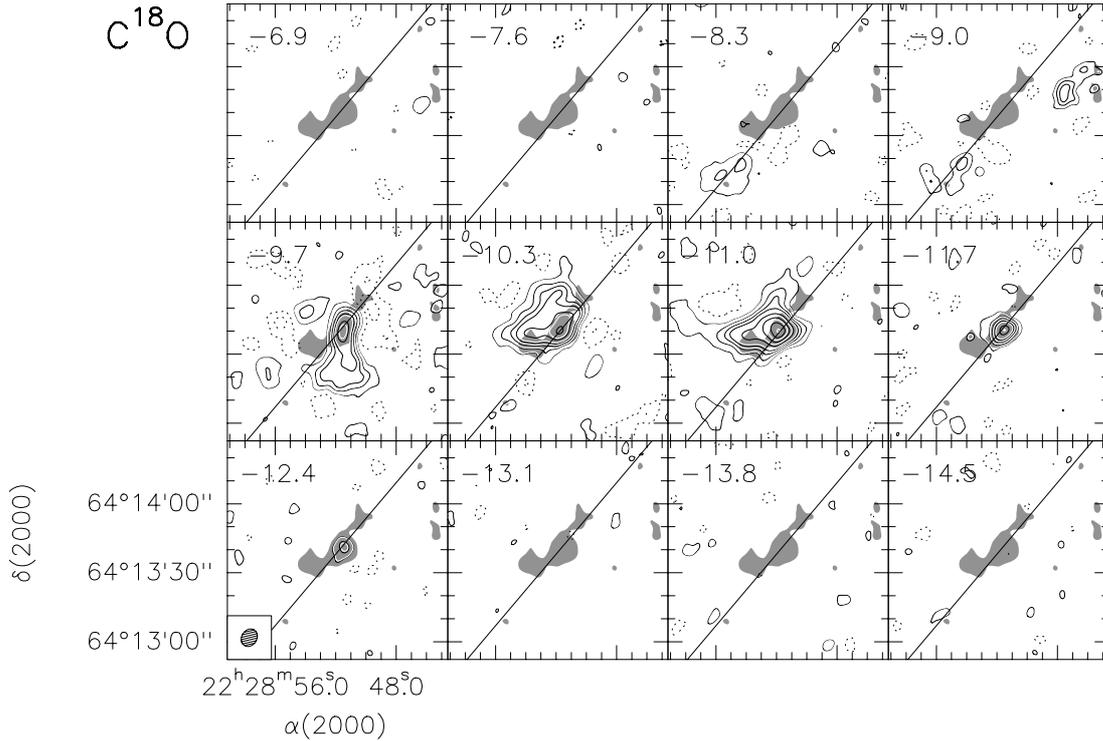
Fig. 5. Velocity channel maps of the $C^{18}O$ ($J = 1 \rightarrow 0$) emission (*contours*) overlaid on the 2.7 mm continuum emission (*greyscale*). The V_{LSR} of L1206 is -11 km s^{-1}. The central velocity of each channel is indicated at the upper left corner of each panel. The 1σ noise in 1 channel is 40 mJy beam^{-1}. Contour levels are -7σ, -3σ, 3 to 15 times σ by steps of 4σ, and 15 to 39 times σ by steps of 8σ. The conversion factor from Jy beam^{-1} to K is 1.93. The synthesized beam is drawn in the bottom left corner of the bottom left panel. The line outlines the direction of the CO outflow (see Fig. 2).

3.4. HC₃N emission

The HC$_3$N ($J = 12 \rightarrow 11$) transition has a high critical density (8×10^5 cm^{-3}: Chung et al. 1991), which makes it an even better tracer of high density regions than, e.g., CS ($J = 1 \rightarrow 0$) and CS ($J = 2 \rightarrow 1$). Figure 7 shows the velocity channel maps for the HC$_3$N ($J = 12 \rightarrow 11$) emission toward the core of L1206, around the systemic velocity, $V_{LSR} \simeq -11$ km s^{-1}, overlaid on the continuum emission. The emission integrated over the velocity interval $(-11.7, -9.7)$ km s^{-1} is shown in the bottom panel of Fig. 6. The gas emission at velocities of -11.0 and -11.7 km s^{-1} is very compact and peaks at the position of the continuum intermediate-mass protostar OVRO 2. At these velocities, an emission tail is also visible toward the southeast, which is associated with the continuum sources OVRO 3 and 4. For the redshifted velocities -9.7 and -10.3 km s^{-1}, the emission shows a less compact and more elongated morphology (see Fig. 7). The emission peak of the gas at these two redshifted velocities is located southeastwards of OVRO 2, in the same direction as the the CO redshifted lobe (see Fig. 2). As can be seen in the channel and integrated emission maps, the gas emission is elongated along the direction of the CO molecular outflow. This morphological correlation between the outflow and dense protostellar material is similar to the case of the low-mass Class 0 source in L1157 (Beltrán et al. 2004a), mapped in the same molecular line HC$_3$N ($J = 12 \rightarrow 11$). However, for L1206, our OVRO observations did not provide us with enough angular resolution to trace the apparent base of the outflow conical cavities in HC$_3$N as traced by the CO, and to more clearly map the "cross-like" pattern characteristic of the interaction between the molecular outflow and the protostellar envelope. The integrated

HC$_3$N emission has a flux density $\sim$10.5 Jy beam^{-1} km s^{-1} and a deconvolved size of 8″.8 or $\sim$8000 AU.

The kinematics of HC$_3$N toward the core of L1206 can be seen in the PV cut done along the direction of OVRO 2 molecular outflow (see Fig. 8). The emission shows two peaks, one at the position of the continuum source, which corresponds to offset position zero, at the systemic velocity, and the other one is $\sim$5″.5 southeast from the central position, at a velocity of $\sim$$-10.3$ km s^{-1}. In addition to this redshifted emission peak, an excess of emission, or emission tail, is also clearly visible, extending further away than the CO redshifted lobe (up to $\sim$27″ or $\sim$24 600 AU southeastwards of OVRO 2), and reaching velocities up to $\sim$$-9$ km s^{-1}.

4. Analysis and discussion

4.1. Dust emission

The masses of the cores given in Table 2 have been estimated assuming that the dust emission is optically thin, by using

$$M_{clump} = \frac{g\,S_\nu\,d^2}{\kappa_\nu\,B_\nu(T_d)},\tag{1}$$

where S_ν is the flux density, d is the distance to the source, κ_ν is the dust mass opacity coefficient, g is the gas-to-dust ratio, and $B_\nu(T_d)$ is the Planck function for a blackbody of dust temperature T_d, all measured at $\nu = 112.5$ GHz. We adopted $\kappa_{112.5} = 0.20$ cm^2 g^{-1} ($\kappa_0 = 1$ cm^2 g^{-1} at 250 GHz: Ossenkopf & Henning 1994), $g = 100$, and $T_d = 33$ K for all the sources. Estimates of T_d have been obtained by fitting a grey-body to the IRAS fluxes at 60 and 100 μm and to the sum of fluxes of

Table 3. Properties of the CO outflow.

Lobe	v^a (km s^{-1})	M^b ($10^{-2} M_\odot$)	P^c ($M_\odot$ km s^{-1})	E^c (10^{43} erg)	$\dot{P}^c$ ($M_\odot$ km s^{-1} yr^{-1})
Blue	[−30.5, −13.5]	8.3	0.60	4.78	7.5×10^{-5}
Red^d	[−8.5, −2.5]	0.2	0.01	0.03	2.3×10^{-6}
Total		8.5	0.61	4.81	7.7×10^{-5}

^{a} Range of outflow velocities. Momenta and kinetic energies are calculated relative to the cloud velocity, which is taken to be $V_{\mathrm{LSR}} = -11$ km s^{-1}.
^{b} Assuming an excitation temperature of 24 K. ^{c} Velocity not corrected for inclination. ^{d} The outflow has only been detected for this velocity range.
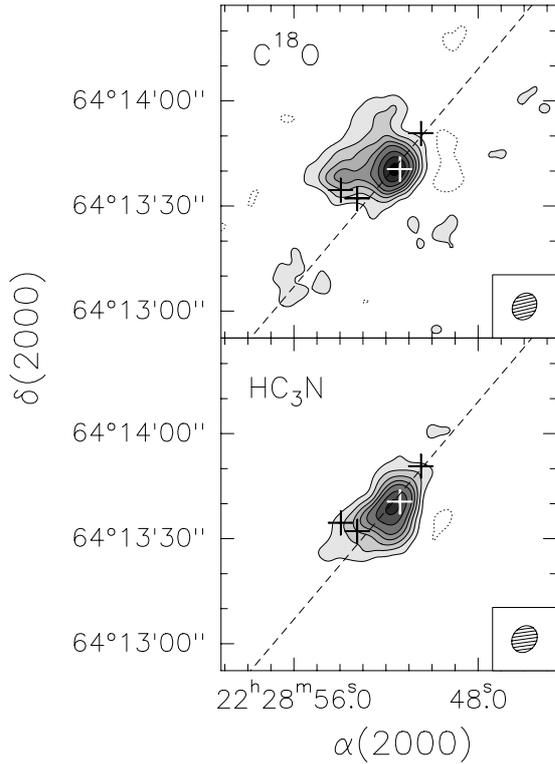
Fig. 6. *Top*: integrated intensity map of the C^{18}O ($J = 1 \rightarrow 0$) emission over the velocity interval $(-12.4, -8.3)$ km s^{-1} toward L1206. Contour levels are -0.36, 0.36 to 1.8 Jy beam^{-1} km s^{-1} by steps of 0.36 Jy beam^{-1} km s^{-1}, and 1.8 to 3.6 Jy beam^{-1} km s^{-1} by steps of 0.6 Jy beam^{-1} km s^{-1}. *Bottom*: integrated intensity map of the HC$_3$N ($J = 12 \rightarrow 11$) emission over the velocity interval $(-11.7, -9.7)$ km s^{-1}. Contour levels are -0.3, 0.3 to 1.5 Jy beam^{-1} km s^{-1} by steps of 0.3 Jy beam^{-1} km s^{-1}, and 1.5 to 2.5 Jy beam^{-1} km s^{-1} by steps of 0.5 Jy beam^{-1} km s^{-1}. The crosses show the positions of the 2.7 mm continuum sources detected in the region. The dashed line indicates the direction of the CO outflow. The synthesized beam is drawn in the bottom right corner of each panel.

the 4 clumps at 2.7 mm We have neglected the IRAS fluxes at 12 and 25 μm in the fit. The reason for this choice is that two components are known to be present in the SEDs of luminous YSOs (see Sridharan et al. 2002): one associated with compact, hot gas and dominating the 12 and 25 μm fluxes; the other due to colder material, contributing to the 60 and 100 μm emission. The latter is the one of interest to us because we want to estimate the temperature of the low-temperature dust in the circumstellar envelope of the sources. Adopting a dust absorption coefficient proportional to ν^2, we found $T_{\mathrm{d}} \simeq 33$ K. This is the same value obtained by Sugitani et al. (2000), fitting the fluxes at 2 mm, 100 μm, and 60 μm, with a dust absorption coefficient proportional to $\nu^{1.8}$.

The mass estimated for OVRO 2 is 14.2 $M_\odot$, while for the other sources the mass is 1.6, 1.8, and 2.2 $M_\odot$ for OVRO 1, OVRO 3, and OVRO 4, respectively. Therefore, OVRO 2, which has a circumstellar mass consistent with the YSO being an intermediate-mass source, accounts for most of the mass toward the core of L1206. The mass estimates of the other sources suggest that they are low-mass YSOs. We also estimated the average H$_2$ volume density, $n(\mathrm{H}_2)$, and column density, $N(\mathrm{H}_2)$, of the sources by assuming spherical symmetry and a mean molecular mass per H$_2$ molecule of $2.8 m_{\mathrm{H}}$. The values are given in Table 2.

4.2. Physical parameters of the CO outflow

Assuming that the CO emission is in LTE and is optically thin, the mass of the gas associated with the outflow detected in the region can be calculated by using

$$\left(\frac{M}{M_\odot}\right) = 2.3 \times 10^{-5} \frac{T_{\mathrm{ex}} + 0.93}{\exp(-5.59/T_{\mathrm{ex}})} \left(\frac{d}{\mathrm{kpc}}\right)^2$$
$$\times \int \left(\frac{S_\nu}{\mathrm{Jy}}\right)\left(\frac{dv}{\mathrm{km\,s}^{-1}}\right), \tag{2}$$

where T_{ex} is the CO excitation temperature, d is the distance in kpc, and S_ν is the line flux density measured in Jy. An excitation temperature of 24 K has been estimated from the CO ($J = 2 \rightarrow 1$) antenna temperature, $T_{\mathrm{A}}^* = 15.4$ K, obtained by Wilking et al. (1989), which corresponds to $T_R = 18.6$ K (Kutner & Ulich 1981) for an efficiency $\eta_{\mathrm{c}} = 1$ and a forward scattering and spillover efficiency $\eta_{\mathrm{fss}} = 0.83$. We assumed an [H$_2$]/[CO] abundance ratio of 10^4 (e.g., Scoville et al. 1986), and a mean atomic mass per H atom $\mu = 1.4$. In Table 3 we give the masses, the CO momentum, the kinetic energy, and the momentum rate in the outflow. We also report the range of outflow velocities for the outflow. Note that due to the fact that some emission is resolved out by the interferometer and the absorption by the ambient cloud, the masses calculated should be considered as lower limits. There is also the possibility that the CO is optically thick in portions of the flow, although the correction for opacity should be small, as one would expect that for high outflow velocities the material is optically thin. Finally, it should be taken into account the integration range chosen, which could make that part of the outflow at low velocities is not counted. Note that the momentum, kinetic energy, and momentum rate in the outflow have not been corrected for the (unknown) inclination angle, i, of the flow with respect to the plane of the sky. In the case of correcting for inclination, the velocities should be divided by $\sin i$. The values of the mass, momentum, kinetic energy, and momentum rate are smaller than the values estimated for other intermediate-mass molecular outflows, such as IRAS 20050+2720 (Bachiller et al. 1995), IRAS 21391+5802 (Beltrán et al. 2002), HH288 (Gueth et al. 2001), L1641S (see references in Anglada 1995 and Wu et al. 2004), or NGC 2071 (Snell et al. 1984), as can be seen
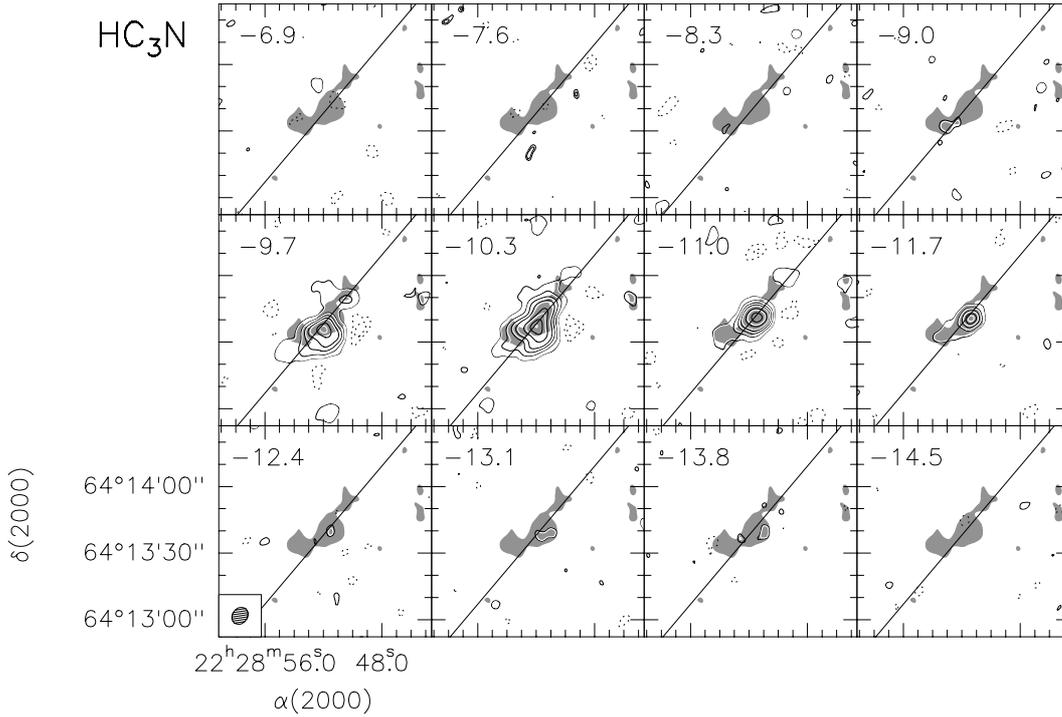
Fig. 7. Velocity channel maps of the HC$_3$N ($J = 12 \rightarrow 11$) emission *(contours)* overlaid on the 2.7 mm continuum emission *(greyscale)*. The V_{LSR} of L1206 is -11 km s^{-1}. The central velocity of each channel is indicated at the upper left corner of each panel. The 1σ noise in 1 channel is 40 mJy beam^{-1}. Contour levels are -5σ, -3σ, 3 to 15 times σ by steps of 4σ, and 15 to 31 times σ by steps of 8σ. The conversion factor from Jy beam^{-1} to K is 1.88. The synthesized beam is drawn in the bottom left corner of the bottom left panel. The line outlines the direction of the CO outflow (see Fig. 2).
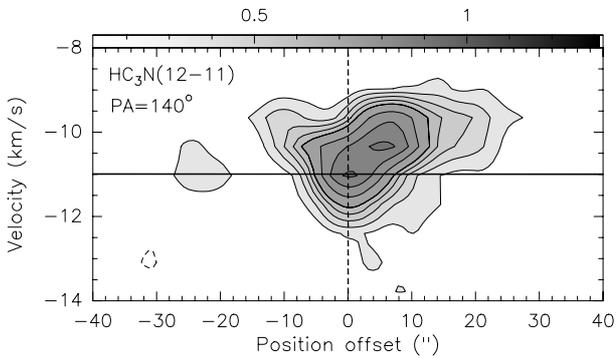
Fig. 8. PV plot of the HC$_3$N ($J = 12 \rightarrow 11$) emission along the major axis, PA = 140°, of the molecular outflow. The position offset is relative to the projection of the 2.7 mm continuum emission peak onto the outflow axis, α(J2000) = 22^{h}28^{h}51^{s}52, δ(J2000) = $+64°13'41''7$. Contours are -0.12, 0.12 to 0.6 Jy beam^{-1} by steps of 0.12 Jy beam^{-1}, and 0.6 to 1.32 Jy beam^{-1} by steps of 0.24 Jy beam^{-1}. The horizontal line marks the systemic velocity, $V_{LSR} = -11$ km s^{-1}.

in Table 4, and are more consistent with the values derived for low-mass outflows (e.g., Cabrit & Bertout 1992; Anglada 1995; Bontemps et al. 1996; Lee et al. 2000, 2002). The reason for this could be the weakness of the redshifted lobe of the OVRO 2 flow, which hardly contributes to the mass, momentum, and energy of the molecular outflow. A possible explanation for the weakness of the redshifted lobe is given in Sect. 4.6.

4.3. Envelope mass from gas emission

One of the major problems when using the gas emission to estimate the mass of the molecular core is the uncertainty of the gas abundance relative to molecular hydrogen. Therefore, due to these uncertainties, instead of measuring the mass of the gas toward the intermediate-mass protostar OVRO 2 from the C^{18}O or HC$_3$N emission, it is better to estimate the fractional abundance of C^{18}O and HC$_3$N. To do that, we integrated the gas emission in the same area ($\sim$162 arcsec^2) used to estimate the mass of the gas from the continuum dust emission, and assumed that the mass toward OVRO 2 derived from the HC$_3$N is the same as that derived from the 2.7 mm continuum emission; that is, 14.2 $M_\odot$. Following the derivation of Scoville et al. (1986), and assuming optically thin emission, the C^{18}O beam averaged column density is given by

$$\langle N \rangle = 4.6 \times 10^{13} \frac{(T_{ex} + 0.878)}{e^{-5.27/T_{ex}}} \int T_B \, dv \, \text{cm}^{-2}, \qquad (3)$$

where T_{ex} is the excitation temperature, and $\int T_B dv$ is the integrated brightness temperature of the C^{18}O ($J = 1 \rightarrow 0$) emission in K km s^{-1}. Assuming an excitation temperature $T_{ex} = 24$ K, the estimated C^{18}O ($J = 1 \rightarrow 0$) abundance relative to molecular hydrogen is 3×10^{-8} toward OVRO 2, a value that is $\sim$6 to 13 times lower than typical fractional abundances estimated toward molecular clouds, 1.7–4×10^{-7} (Frerking et al. 1982; Kulesa et al. 2005). Even if one takes into account the uncertainties up to a factor of 5 introduced in the mass estimates by the different dust opacity laws used, the value of the abundance derived toward OVRO 2 would be lower than the typical fractional abundances. In particular, it would be clearly inconsistent with the abundance of 4×10^{-7} derived by Kulesa et al. (2005) in the ρ Ophiuchi molecular cloud. The excitation temperature value adopted cannot account for the abundance difference, as the abundance estimate is not significantly affected by the excitation temperature (the abundance would be 2.7×10^{-8} for $T_{ex} = 20$ K,

Table 4. Properties of intermediate-mass outflows.

Outflow	M ($M_\odot$)	P ($M_\odot$ km s^{-1})	E (10^{45} erg)	$\dot{P}$ ($M_\odot$ km s^{-1} yr^{-1})
IRAS 20050+2720[a]	1.7	25.4	7.7	$\sim 5.0 \times 10^{-3}$
IRAS 21391+5802[b]	0.14	3.6	1.2	1.4×10^{-3}
HH288[c]	11	385	6.7	1.4×10^{-2}
L1641S[d]	1.4	37	0.3	5.3×10^{-4}
NGC 2071[e]	10	81	8.5	5.1×10^{-3}

[a] The parameters correspond to the whole emission of the different outflow lobes detected in IRAS 20050+2720 (Bachiller et al. 1995). [b] Beltrán et al. (2002). [c] Because of the difficulty of treating each outflow separately, the parameters correspond to the whole emission, thus including the two outflows detected in HH228 (Gueth et al. 2001). [d] Anglada (1995) and Wu et al. (2004). [e] Snell et al. (1984).

Table 5. C^{18}O ($J = 1 \to 0$), and HC$_3$N ($J = 12 \to 11$) line and physical parameters toward the continuum peak position of OVRO 2 in L1206

Molecule & transition	$V_{\rm LSR}$ (km s^{-1})	$FWHM$ (km s^{-1})	$T_{\rm B}$ (K)	$\int T_{\rm B}\,dV$ (K km s^{-1})	θ^a (arcsec)	$M_{\rm vir}^b$ ($M_\odot$)
C^{18}O ($J = 1 \to 0$)	-10.74 ± 0.02	2.34 ± 0.04	2.94 ± 0.31	7.31 ± 0.13	8.8	10.6–14.2
HC$_3$N ($J = 12 \to 11$)	-10.86 ± 0.03	1.83 ± 0.07	2.68 ± 0.10	5.22 ± 0.17	11.4	13.4–17.8

[a] Deconvolved geometrical mean of the major and minor axes of the half-peak intensity contour. [b] Estimated from Eq. (5) for typical density distributions with $p = 2.0$–1.5.

and 4×10^{-8} for $T_{\rm ex} = 40$ K). One should also take into account opacity effects, in case the C^{18}O emission is optically thick. In such a case, the gas mass and the C^{18}O ($J = 1 \to 0$) abundance relative to molecular hydrogen would be higher. In case the opacity of the gas is $\tau \gtrsim 3$, the main beam brightness temperature can be given by $T_{\rm mb} \simeq f[J(T_{\rm ex}) - J(T_{\rm bg})]$, where f is the beam filling factor and $T_{\rm bg}$ is the background temperature. For OVRO 2, $T_{\rm mb}$ is 2.94 K (see Table 5) and $T_{\rm ex} = 24$ K. Therefore, the filling factor would be $f = 0.14$, suggesting that the emission is clumpy. However, if the C^{18}O emission were clumpy, such clumps should be visible in the maps done with uniform weighting or with a negative robust parameter, and this is not the case. This means that opacity can be ruled out as being responsible for the mass difference. Therefore, the most plausible explanation to account for the low C^{18}O ($J = 1 \to 0$) abundance appears to be CO depletion toward OVRO 2.

Regarding the HC$_3$N emission, the uncertainties in the HC$_3$N abundance relative to molecular hydrogen (see, e.g., Hasegawa et al. 1986) can make the mass estimates vary up to 3 orders of magnitude. Chung et al. (1991) estimate abundances of $(2-7) \times 10^{-10}$ in massive dense cores, while that of a low-mass dense core, L1551, has been estimated to be 2×10^{-9}. Similar abundances have been estimated by Jørgensen et al. (2004) for a sample of Class 0 and Class I low-mass protostellar envelopes. The average values determined are 3.5×10^{-10} and 3.1×10^{-9}, respectively. However, abundances as low as $\sim 3 \times 10^{-11}$ have been estimated for a sample of 19 low and massive molecular clouds (Vanden Bout et al. 1983), and as high as $\sim 10^{-8}$ for hot cores associated with intermediate- and high-mass stars (de Vicente et al. 2000; Martín-Pintado et al. 2005). Therefore, as done before with the C^{18}O emission, we estimated the fractional abundance of HC$_3$N toward OVRO 2. Following the derivation of Scoville et al. (1986), and assuming optically thin emission, the HC$_3$N beam averaged column density is given by

$$\langle N \rangle = 4.2 \; 10^{10} \frac{(T_{\rm ex} + 0.073)}{e^{-34.06/T_{\rm ex}}} \int T_B \, dv \; {\rm cm}^{-2}, \qquad (4)$$

where $T_{\rm ex}$ is the excitation temperature, and $\int T_B dv$ is the integrated brightness temperature of the HC$_3$N ($J = 12 \to 11$)

emission in K km s^{-1}. Assuming an excitation temperature $T_{\rm ex} = 24$ K, the estimated HC$_3$N abundance relative to molecular hydrogen is 7×10^{-11} toward OVRO 2, a value in the lower end of the range of fractional abundances estimated toward molecular clouds.

### 4.4. Physical parameters of the dense core toward OVRO 2

Table 5 lists the fitted parameters for C^{18}O ($J = 1 \to 0$) and HC$_3$N ($J = 12 \to 11$) toward the 2.7 mm continuum peak position of OVRO 2. The spectra and the corresponding Gaussian fits are shown in Fig. 9. In Table 5 we also give the deconvolved size and the virial mass estimated assuming a spherical clump with a power-law density distribution $\rho \propto r^{-p}$, and neglecting contributions from magnetic field and surface pressure. In such a case, the virial mass can be computed from the expression (see, e.g., MacLaren et al. 1988):

$$\left(\frac{M_{\rm vir}}{M_\odot} \right) = 0.305 \, \frac{5 - 2p}{3 - p} \left(\frac{d}{\rm kpc} \right) \left(\frac{\theta}{\rm arcsec} \right) \left(\frac{\Delta V}{\rm km\,s^{-1}} \right)^2, \qquad (5)$$

where p is the density distribution power-law index, d is the distance, θ is the deconvolved size of the source, and ΔV is the line width. The line widths, which have been estimated from the Gaussian fits to the spectra, coincide with the line widths estimated from the second order moment maps. The virial masses estimated from C^{18}O and HC$_3$N are 13.4–17.8 $M_\odot$, and 10.6–14.2 $M_\odot$, respectively, for typical density distributions with $p = 2.0$–1.5. Such values are consistent with the mass derived from the continuum. However, the mass of the central protostar has not been taken into account in this calculation. Therefore, in fact, the total mass (circumstellar plus protostar) of OVRO 2 is probably higher than the virial mass, suggesting that this object is likely undergoing collapse, as one would expect from a very young stellar object.

4.5. Intermediate-mass protostars and their outflows

The millimeter continuum emission around IRAS 22272+6358A has been resolved into four different clumps (see
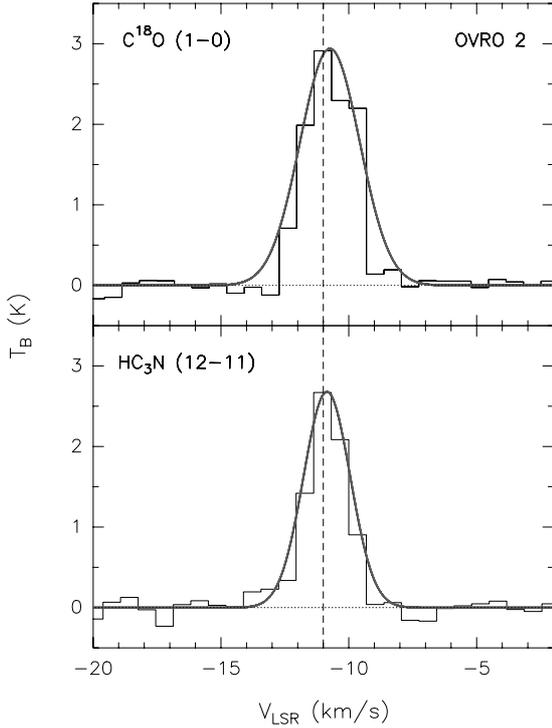
Fig. 9. $C^{18}O$ ($J = 1 \rightarrow 0$) (*top*) and HC_3N ($J = 12 \rightarrow 11$) (*bottom*) spectra obtained at the position of OVRO 2 in L1206. The continuum has been subtracted. The 1σ level in one channel is 0.10 K. The conversion factor is 1.93 K/Jy beam^{-1} for $C^{18}O$ and 1.88 K/Jy beam^{-1} for HC_3N. The thick grey profiles are the Gaussian fits to the spectra. The dashed vertical line indicates the systemic velocity of -11 km s^{-1}.

Fig. 1): an intermediate-mass source, OVRO 2, and three less massive and smaller objects, OVRO 1, OVRO 3, and OVRO 4. This situation very closely resembles the scenario around IRAS 21391+5802, which is located in the bright-rimmed cloud IC 1396N. In this case, the millimeter and centimeter emissions have been resolved into an intermediate-mass source, BIMA 2, which is the YSO associated with IRAS 21391+5802, surrounded by two (Beltrán et al. 2002) or maybe three (Beltrán et al. 2004b) much less massive YSOs, with different morphologies and properties. As was already mentioned, OVRO 2 is the source associated with IRAS 22272+6358A, has the strongest millimeter emission, and is also the most massive object toward the core of L1206. The source is associated with OH and CH_3OH maser emission (MacLeod et al. 1998), but not with H_2O maser emission (Palla et al. 1991) or with continuum emission at 2 and 6 cm (Wilking et al. 1989; McCutcheon et al. 1991). OVRO 2, as seen in the previous sections, is driving a powerful molecular outflow, which has an estimated kinematical age of the order of a few 10^4 years, which suggests that the powering source is a very young stellar object. The source, which has not been detected at 12 μm by IRAS, has a cold dust temperature, $T_d \simeq 33$ K, and its millimeter emission, which accounts for most of the dust emission in the region, exhibits an extended component that is consistent with an envelope surrounding the source. The circumstellar mass, $M \simeq 14.2 \, M_\odot$, is consistent with the masses in the range 3.5–30 $M_\odot$ found around other intermediate-mass protostars (Fuente et al. 2001; Gueth et al. 2001; Shepherd & Watson 2002), and it is considerably higher than the envelope masses of 1.4–2.3 $M_\odot$ found by Bontemps et al. (1996) for

low-mass Class 0 sources. Therefore, these properties indicate that OVRO 2 is an extremely young, deeply embedded intermediate-mass protostar, with morphology and properties that do not differ significantly from the properties of low-mass counterpart protostars. In fact, the source, which has not been detected at J, H, K, L, or L' bands (Ressler & Shure 1991), has been classified as a heavily extinguished Class I object with an optically thick almost edge-on circumstellar disk. Pezzuto et al. (2002) also classify IRAS 22272+6358A as a Class I object based on its [60–100] μm and [100–170] μm color temperatures, although the low spatial resolution of the Long Wavelength Spectrometer (LWS) on board of the Infrared Space Observatory can cause a high uncertainty in the measured fluxes due to background emission or source confusion inside the LWS beam. On the other hand, taking into account the criterion for Class 0 given by André et al. (1993), $L_{bol}/L_{submm} \lesssim 200$, Sugitani et al. (2000) classify IRAS 22272+6358A as a Class 0-like object since its ratio L_{bol}/L_{submm} is 140. Therefore, OVRO 2 seems to be a very young intermediate-mass object in transition state between Class 0 and I.

To further compare the properties of the intermediate-mass YSO OVRO 2 with the low-mass case, we also checked whether this object is consistent with some correlations between source and outflow properties found for low-mass young objects. As already mentioned in Sect. 4.2, although L_{bol} and the dust continuum emission toward OVRO 2 indicate that the source is an intermediate-mass object, the properties of the molecular outflow are more consistent with those derived for low-mass protostars. Therefore, we checked for the correlation between the circumstellar envelope mass and the momentum rate in the CO outflow given by Bontemps et al. (1996) for low-mass embedded YSOs. For this correlation, Bontemps et al. (1996) correct the observed momentum rate of the CO outflow, $\dot{P}_{obs}$, by a factor 10, $\dot{P} \simeq 10 \times \dot{P}_{obs}$, to take into account projection and optical depth effects. After applying the same correction factor to the momentum rate of the OVRO 2 outflow, we found that OVRO 2 agrees well with the correlation, as well as with the intermediate-mass protostar IRAS 21391+5802 (Beltrán et al. 2002). Bontemps et al. (1996) also find a correlation between the normalized outflow momentum rate or outflow efficiency, $\dot{P}c/L_{bol}$, and the normalized envelope mass, $M/L_{bol}^{0.6}$. For IRAS 22272+6358A, the estimated bolometric luminosity is $L_{bol} \simeq 1200 \, L_\odot$ (Sugitani et al. 1989). However, this estimate includes the whole region around the IRAS catalogue position. Thus, to derive a bolometric luminosity for OVRO 2, we used the relationship between the momentum rate and the bolometric luminosity given by Bontemps et al. (1996), and we inferred a luminosity of $L_{bol} \simeq 580 \, L_\odot$. By using this luminosity, we found that the source has an outflow efficiency consistent with those of low-mass Class I sources, and also with that of IRAS 21391+5802, if one estimates the bolometric luminosity of the latter from the outflow momentum rate by using the Bontemps et al. (1996) correlation. Both intermediate-mass sources, OVRO 2 and IRAS 21391+5802, fit the correlation of outflow efficiency and envelope mass found by Bontemps et al. (1996) well, and both lie in the limit between the Class 0 and I regions of this diagram. Furthermore, another correlation fitted well by both sources is the one between the radio continuum luminosity at centimeter wavelengths and the momentum rate of the outflow not corrected for inclination obtained by Anglada (1996). This correlation is in agreement with the predictions of a simple model of shock ionization in a plane-parallel geometry (Curiel 1987, 1989), which would be able to produce the required ionization in thermal radio jets.

Intermediate-mass outflows have been proposed to be more complex and to have more chaotic morphologies than those found toward low-mass protostars (e.g., NGC 7129: Fuente et al. 2001). However, this does not seem to be the case of the OVRO 2 molecular outflow in L1206. In addition, unlike the NGC 7129 FIRS1 outflow, the collimation of the OVRO 2 outflow is very high, even at low velocities, similar to the intermediate-mass outflow driven by BIMA 2 in IC 1396N (Beltrán et al. 2002) or to the low-mass protostellar flow in HH 211 (Gueth & Guilloteau 1999). As already discussed by Beltrán et al. (2002) for the BIMA 2 outflow in IC 1396N, given that the outflows are usually more energetic for higher mass objects, that the dust emission is often resolved into more than one object, and that intermediate- and high-mass sources are embedded in larger amounts of material, it is to be expected that the interactions between the high-velocity gas and the circumstellar material will be more dramatic, disrupting and pushing more material. Therefore, the complexity of the molecular outflows driven by intermediate-mass protostars is likely a result of the more complex protostellar environment itself.

4.6. Interaction of the molecular cloud with the ionized bright-rimmed cloud

The most striking features of the morphology of the molecular outflow powered by OVRO 2 are the weakness and small size of the redshifted lobe as compared to the blueshifted one (see Fig. 2); that is, the nearly lack of outflowing material south of the YSO OVRO 2. The existence of unipolar, or primarily one-sided, molecular outflows have also been reported for other low- and intermediate-mass star-forming regions (e.g., NGC 2024/FIR5: Richer et al. 1989; HH 46-47: Chernin & Masson 1991; L1641-S3: Stanke et al. 2000; HH 300: Arce & Goodman 2001). Taking into account the fact that the molecular outflow consists of ambient gas that is swept up from a position close to where it is observed, a possible explanation for the morphology of the OVRO 2 outflow could be that the redshifted lobe breaks out of the molecular cloud. That is, the redshifted wind passes into a region where there is no, or little, molecular material to be swept up. A similar scenario has been suggested to explain the near unipolarity of the HH 46-47 molecular outflow (Chernin & Masson 1991).

Figure 10 shows the superposition of the VLA[1] 6 cm emission (archive data) of the bright-rimmed cloud (BRC 44) on the red image of the Digitized Sky Survey 2 toward L1206. The 6 cm emission is spatially coincident with the L1206 dark cloud. The optical bright rim, which is a diffuse HII region, coincides with the southern part of the 6 cm emission. This suggests that the HII region is located in the background with respect to L1206. Therefore, a more plausible explanation for the morphology of the molecular outflow powered by OVRO 2 could be photodissociation of the redshifted (southern) lobe. The ionization-shock front probably lies very close to the southern redshifted outflow, and thus, any redshifted (southern) ejected material could be destroyed by the intense radiation field at the ionization front. Photodissociation has also been proposed as an explanation of the unipolarity of the NGC 2024/FIR5 outflow (Richer et al. 1989). To check the validity of this possible scenario, we have estimated the internal pressure of the molecular gas in the L1206 cloud and compared it with the Ionized Boundary Layer
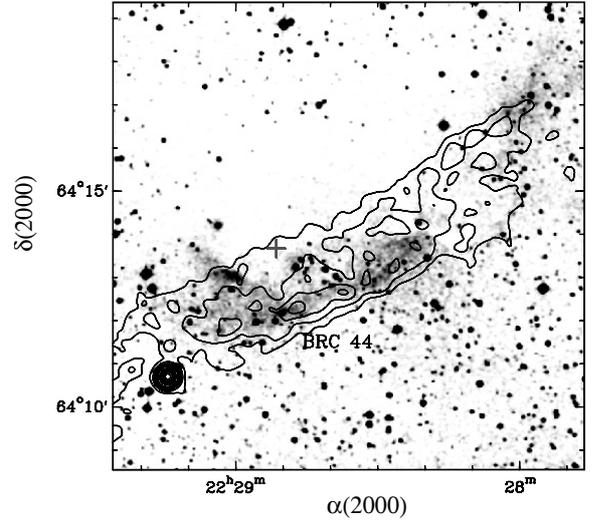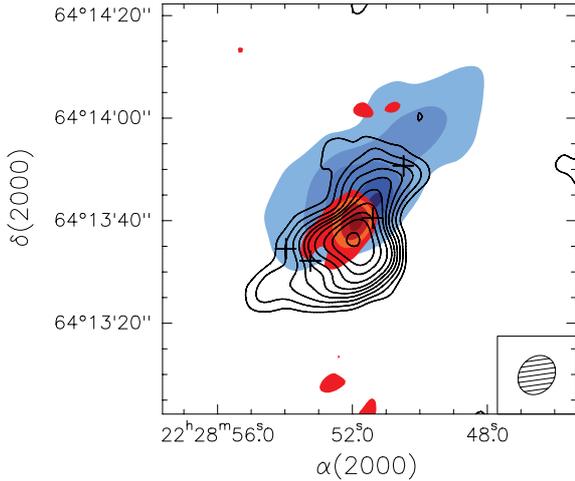

Fig. 10. VLA map of the 6 cm emission *(contours)* overlaid with an optical image from the Digitized Sky Survey 2 *(colors)* of BRC 44. The contours are 0.2, 0.4, 0.7, 1.0, 1.5, 2.5, 3.5, 4.5, 5.5, and 6.5 mJy beam^{-1}. The cross marks the position of the 2.7 mm continuum source OVRO 2.

(IBL) pressure. The IBL pressure divided per Boltzmann's constant, P_i/k_B, estimated from the NRAO/VLA sky survey (NVSS) data at 20 cm for this bright-rimmed cloud is 8.5×10^6 cm^{-3} K (Morgan et al. 2004)[2]. Following Morgan et al. (2004), we have estimated the internal molecular pressure, $P_m = \sigma^2 \rho_m$, where σ is the velocity dispersion, which can be given in terms of the observed line width Δv as $\sigma^2 = (\Delta v)^2/(8 \ln 2)$, and ρ_m is the density of the molecular gas. The velocity dispersion has turbulent and thermal contributions. However, as the clouds are composed mostly of cold gas, one would expect the thermal contribution to be almost negligible. Sugitani et al. (1989) derive $\rho_m = 2.1 \times 10^4$ cm^{-3} from ^{13}CO observations, but they do not give the value of the observed line width. Thus, using the ^{13}CO line width derived by Ridge et al. (2003), we obtained $P_m/k_B \simeq 3.7 \times 10^6$ cm^{-3} K. If one uses ρ_m derived from the observations of Ridge et al. (2003) by assuming spherical symmetry of the cloud, the values of P_m/k_B are 1.8×10^6 and 5.0×10^6 cm^{-3} K for ^{13}CO and C^{18}O, respectively. In summary, the internal molecular pressure ranges from 1.8 to 5.0×10^6 cm^{-3} K, depending on the values of the density and line width adopted, but in any case, it is always smaller than the IBL pressure. Thus, the cloud seems to be underpressured with respect to the IBL, and therefore, one might expect photoionization shocks and the ionization front to be propagating into the cloud interior, compressing, heating, and photodissociating the molecular gas. Definitively, the possibility exists that photodissociation is responsible for the morphology of the molecular outflow, and therefore, that the HII region is actually eating the outflow.

---

[1] The National Radio Astronomy Observatory is a facility of the National Science Foundation operated under cooperative agreement by Associated Universities, Inc.

[2] After this paper went to press, we realized that there is an error in the Morgan et al. (2004) paper (L. K. Morgan 2006, private communication), and that the value quoted for the IBL pressure of the cloud should be lower. This brings the pressure difference in the cloud to approximate equilibrium, and therefore, right now, the ionization front would probably not be traveling towards the protostar, but stalled. This does not affect the main conclusion of the work; namely, the fact that the morphology of the L1206 outflow is the result of photoionization from the HII region.

Fig. 11. Overlap of the intensity map of the HC$_3$N ($J = 12 \rightarrow 11$) emission (*contours*), integrated over the velocity interval (-10.3, -9.7) km s^{-1}, on the CO ($J = 1 \rightarrow 0$) blueshifted emission (*blue colors*), integrated over the (-19.5, -13.5) km s^{-1} velocity interval, and the redshifted emission (*red colors*), integrated over the (-8.5, -2.5) km s^{-1} velocity interval. Contour levels are 0.12, 0.2, 0.28, 0.36, 0.44, 0.52, 0.64, 0.80, 0.96, and 1.2 Jy beam^{-1} km s^{-1} (*contours*), 1.5, 5.5, 9.5, 13.5, and 17.5 Jy beam^{-1} km s^{-1} (*blue colors*), and 0.54, 1.08, 1.62, and 2.16 Jy beam^{-1} km s^{-1} (*red colors*). The crosses show the positions of the 2.7 mm continuum sources detected in the region. The synthesized beam is drawn in the bottom right corner.

4.7. HC$_3$N enhancement

As already mentioned in Sect. 3.4, the HC$_3$N emission at velocities of -11.0 and -11.7 km s^{-1}, which are close to the cloud velocity, is very compact and traces the same material as the continuum emission at 2.7 mm; that is, sources OVRO 2, 3, and 4 (see Fig. 7). On the other hand, at velocities of -9.7 and -10.3 km s^{-1}, which are redshifted with respect to the cloud velocity, the HC$_3$N emission is elongated in the same direction as the CO molecular outflow and peaks south of OVRO 2 (see Figs. 7 and 11). As was already done in Sect. 4.3 toward OVRO 2, we estimated the HC$_3$N fractional abundance toward the red lobe by integrating the gas and the continuum emission in the same area, and assuming that the mass of the gas derived from HC$_3$N is the same as that derived from the continuum. The maximum HC$_3$N fractional abundance southwards of OVRO 2 is $(2-3) \times 10^{-10}$, which compared to 7×10^{-11} estimated toward OVRO 2, indicates that the emission is enhanced toward the south. The correlation between the dense gas and the molecular outflow suggests that the latter could be responsible for the southern HC$_3$N enhancement as a result of shocks that would compress and heat the dense gas. Shock-enhancement of the HC$_3$N abundance has also been detected toward L1157 (Bachiller & Pérez-Gutiérrez 1997; Beltrán et al. 2004a). This hypothesis seems to be supported by the HC$_3$N spectrum at the position of the redshifted peak (see Fig. 12), which is very different from the spectrum at the position of OVRO 2 (Fig. 9). Note, however, that the velocity of the HC$_3$N gas is somewhat lower than that of the CO emission at the same location. This suggests that high velocity material has a lower density, and would thus not be seen in HC$_3$N.

One should notice that, although the HC$_3$N is well correlated with the molecular outflow, the enhancement of HC$_3$N is mainly found toward the southern redshifted lobe instead of toward the stronger northern blueshifted one, as one would expect.
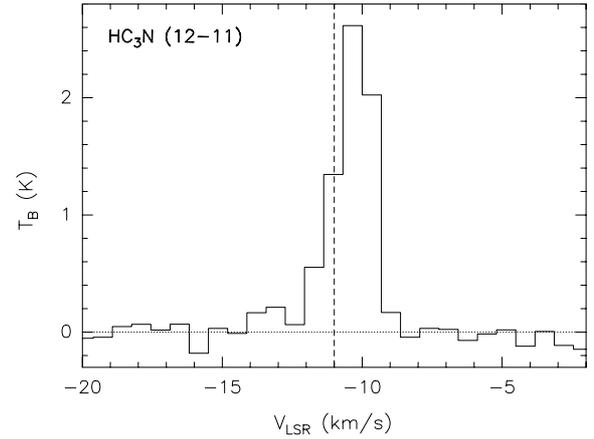
Fig. 12. HC$_3$N ($J = 12 \rightarrow 11$) spectrum obtained at the position of the southern redshifted peak seen at velocities of -9.7 and -10.3 km s^{-1} (see Sect. 4.7). The dashed vertical line indicates the systemic velocity of -11 km s^{-1}.

Furthermore, the peak is found for redshifted velocities with respect to the cloud. One possible explanation for this is that, as mentioned in the previous section, the region southeastern of OVRO 2 is closer to the bright rim and the ionization front, probably located in the background. Therefore, it is possible that the shock front preceding the ionization front has compressed and heated the neutral gas, helping to enhance the HC$_3$N abundance. This would support our hypothesis that the photoionization front that is coming after the shock front is the responsible for the weakness and small size of the redshifted southern lobe. It is worth noticing that once the photoionization front reaches the position where the HC$_3$N emission is found, there will be a decrease in its abundance as HC$_3$N will be dissociated by the UV photons (e.g., Mon R2: Rizzo et al. 2005).

5. Conclusions

We studied the dust and gas emission at 2.7 mm toward IRAS 22272+6358A, an intermediate-mass source embedded in the core of the bright-rimmed cloud L1206, with the OVRO Millimeter Array .

The 2.7 mm continuum emission has been resolved into four sources, OVRO 1, OVRO 2, OVRO 3, and OVRO 4. The strongest source at millimeter wavelengths is OVRO 2, which is most likely the YSO associated with IRAS 22272+6358A, and it is probably the driving source of the CO molecular outflow detected in the region. The millimeter emission of OVRO 2 shows two components, a centrally peaked source, which has a diameter of $\sim$3200 AU at the half-peak intensity contour of the dust emission, plus an extended and quite spherical envelope, which has a size of $\sim$11 800 AU. The mass of OVRO 2, which has been estimated from the dust continuum emission, is 14.2 $M_\odot$. The dust emission morphology and properties of OVRO 2, which are consistent with those of low-mass counterpart protostars, indicate that it is an extremely young, deeply embedded intermediate-mass protostar, probably in transition state between Class 0 and I. The sources OVRO 3 and 4 have a similar deconvolved size, $\sim$5000 AU, and mass, $\sim$2 $M_\odot$, and are probably low-mass protostars. The other source in the region, OVRO 1, could be dusty material entrained by the outflow detected in the region.

The CO ($J = 1 \rightarrow 0$) observations have revealed a very weak southeastern redshifted outflow lobe, which is only visible

at low outflow velocities, and a much stronger northwestern blueshifted lobe, which extends to very high velocities. This collimated molecular outflow is elongated in a direction with PA $\simeq 140°$, and it is clearly centered at the position of OVRO 2. The properties of the outflow are consistent with those of the outflows driven by low-mass YSOs (Bontemps et al. 1996; Anglada 1996).

The internal molecular pressure for the bright-rimmed cloud BRC 44 ranges from 1.8 to 5.0×10^6 cm^{-3} K, and is smaller than the IBL pressure, P_i/k_B, which is 8.5×10^6 cm^{-3} K (Morgan et al. 2004)[3]. This suggests that the cloud is underpressured with respect to the IBL, and therefore, one might expect photoionization shocks and the ionization front to be propagating into the cloud interior, compressing, heating, and photodissociating the molecular gas. Therefore, photodissociation could explain the weakness of the redshifted lobe and the morphology of the molecular outflow, suggesting a scenario where the HII region would be, in fact, eating the redshifted outflow lobe.

The spatial correlation between the outflow and the elongated dense protostellar material, as traced by HC$_3$N ($J = 12 \rightarrow 11$), suggests an interaction between the molecular outflow and the protostellar envelope. Shocks produced by the molecular outflow, and possibly by the shock front preceding the photoionization front coming from the bright rim, would be responsible for the southern enhancement of the HC$_3$N abundance for redshifted outflow velocities.

The C^{18}O abundance relative to molecular hydrogen estimated toward OVRO 2 is 3×10^{-8}, a value ~6 to 13 times lower than typical fractional abundances estimated toward molecular clouds. The most plausible explanation for such a difference is CO depletion toward OVRO 2. The HC$_3$N abundance relative to molecular hydrogen estimated toward OVRO 2 is 7×10^{-11}.

References

André, P., Ward-Thompson, D., & Barsony, M. 1993, ApJ, 406, 122
Anglada, G. 1995, in Disks, Outflows and Star Formation, ed. S. Lizano, & J. M. Torrelles, RevMexAASC, 1, 67
Anglada, G. 1996, in Radio Emission from the Stars and the Sun, ed. A. R. Taylor, & J. M. Paredes (San Francisco: ASP), ASP Conf. Ser., 93, 3
Arce, H. G., & Goodman, A. A. 2001, ApJ, 554, 132
Bachiller, R. 1996, ARA&A, 34, 111
Bachiller, R., & Pérez Gutiérrez, M. 1997, ApJ, 487, L93
Bachiller, R., Fuente, A., & Tafalla, M. 1995, ApJ, 445, L51
Beltrán, M. T., Girart, J. M., Estalella, R., Ho, P. T. P., & Palau, A. 2002, ApJ, 573, 246
Beltrán, M. T., Gueth, F., Guilloteau, S., & Dutrey, A. 2004a, A&A, 416, 631
Beltrán, M. T., Girart, J. M., Estalella, R., & Ho, P. T. P. 2004b, A&A, 426, 941
Bontemps, S., André, P., Terebey, S, & Cabrit, S. 1996, A&A, 311, 858
Cabrit, S., & Bertout, C. 1992, A&A, 261, 274
Casoli, F., Dupraz, C., Gerin, M., Combes, F., & Boulanger, F. 1986, A&A, 169, 281
Chernin, L. M., & Masson, C. R. 1991, ApJ, 382, L93
Chung, H. S., Osamu, K., & Masaki, M. 1991, JKAS, 24, 217
Crampton, D., & Fisher, W. A. 1974, Publ. Dominion Ap. Obs. Victoria, 14
Curiel, S., Cantó, J., & Rodríguez, L. F. 1987, Rev. Mex. Astron. Astrofís., 14, 595
Curiel, S., Rodríguez, L. F., Cantó, J., et al. 1989, Astrophys. Lett. Commun., 27, 299

de Vicente, P., Martín-Pintado, J., Neri, R., & Colom, P. 2000, A&A, 361, 1058
Frerking, M. A., Langer, W. D., & Wilson, R. W. 1982, ApJ, 262, 590
Fuente, A., Neri, R., Martín-Pintado, J., et al. 2001, A&A, 366, 873
Gueth, F., & Guilloteau, S. 1999, A&A, 343, 571
Gueth, F., Schilke, P., & McCaughrean, M. J. 2001, A&A, 375, 1018
Jørgensen, J. K., Schöier, F. L., & van Dishoeck, E. F. 2004, A&A, 416, 603
Kulesa, C. A., Hungerford, A. L., Walker, C. K., Zhang, X., & Lane, A. P. 2005, ApJ, 625, 194
Hasegawa, T., Hirano, N., Kameya, O., et al. 1986, PASJ, 38, 379
Hogerheijde, M. R., van Dishoeck, E. F., Blake, G. A., & van Langevelde, H. J. 1997, ApJ, 489, 293
Hogerheijde, M. R., van Dishoeck, E. F., Salverda, J. M., & Blake, G. A. 1999, ApJ, 513, 350
Kutner, M. L., & Ulich, B. L. 1981, ApJ, 250, 341
Lee, C.-F., Mundy, L., Reipurth, B., Ostriker, E. C., & Stone, J. M. 2000, ApJ, 542, 925
Lee, C.-F., Mundy, L., Stone, J. M., & Ostriker, E. C. 2002, ApJ, 576, 294
Looney, L. W., Mundy, L. G., & Welch, W. J. 2000, ApJ, 529, 477
MacLaren, I., Richardson, K. Mn., & Wolfendale, A. W. 1988, ApJ, 333, 821
MacLeod, G. C., Scalise, E. Jr., Saedt, S., Galt, J. A., & Gaylard, M. J. 1998, AJ, 116, 1897
McCutcheon, W. H., Sato, T., Dewdney, P. E., & Purton, C. R. 1991, AJ, 101, 1435
Molinari, S., Brand, J., Cesaroni, R., & Palla, F. 1996, A&A, 308, 573
Morgan, L. K., Thompson, M. A., Urquhart, J. S., Wjite, G. J., & Miao, J. A&A, 426, 535
Palla, F., Brand, J., Cesaroni, R., Comoretto, G., & Felli, M. 1991, A&A, 246, 249
Pezzuto, S., Grillo, F., Benedettini, M., et al. 2002, MNRAS, 330, 1034
Richer, J. S., Hills, R. E., Padman, R., & Russell, A. P. G. 1989, MNRAS, 241, 231
Martín-Pintado, J., Jiménez-Serra, I., Rodríguez-Franco, A., Martín, S., & Thum, C. 2005, ApJ, 628, L61
Ossenkopf, V., & Henning, Th. 1994, A&A, 291, 943
Ressler, M. E., & Shure, M. 1991, AJ, 102, 1398
Richards, P. J., Little, L. T., Toriseva, M., & Heaton, B. D. 1987, MNRAS, 228, 43
Richer, J., Shepherd, D. S., Cabrit, S., Bachiller, R., & Churchwell, E. 2000, in Protostars and Planets IV, ed. V. Mannings, A. Boss, & S. Russell (Tucson: University of Arizona Press), 867
Ridge, N. A., Wilson, T. L., Megeath, S. T., Allen, L. E., & Myers, P. C. 2003, AJ, 126, 286
Rizzo, J. R., Fuente, A., & García-Burillo, S. 2005, ApJ, 634, 1133
Scoville, N. Z., Sargent, A. I., Sanders, D. B., et al. 1986, ApJ, 303, 416
Scoville, N. Z., Carlstrom, J. E., Chandler, C. J., Phillips, J. A., et al. 1993, PASP, 105, 1482
Shepherd, D. S. 2005, in Massive Star Birth: A Crossroads of Astrophysics, ed. R. Cesaroni, M. Felli, E. Churchwell, & M. Walmsley (Cambridge: Cambridge University Press), Proc. IAU Symp., 227, 237
Shepherd, D. S., & Churchwell, E. 1996a, 457, 267
Shepherd, D. S., & Churchwell, E. 1996b, 472, 225
Shepherd, D. S., & Watson, A. M. 2002, ApJ, 566, 1
Snell, R. L., Scoville, N. Z., Sanders, D. B., & Erickson, N. R. 1984, ApJ, 284, 176
Sridharan, T. K., Beuther, H., Schilke, P., Menten, & Wyrowski, F. 2002, ApJ, 566, 931
Stanke, Th., McCaughrean, M. J., & Zinnecker, H. 2000, A&A, 355, 639
Sugitani, K., Fukui, Y., Mizuno, A., & Ohashi, N. 1989, ApJ, 342, L87
Sugitani, K., Fukui, Y., & Ogura, K. 1991, ApJS, 77, 59
Sugitani, K., Matsuo, H., Nakano, M., Tamura, M., & Ogura, K. 2000, AJ, 119, 323
Vanden Bout, P. A., Loren, R. B., Snell, R. L., & Wootten, A. 1983, ApJ, 271, 161
Wilking, B. A., Mundy, L. G., Blackwell, J. H., & Howe, J. E. 1989, ApJ, 345, 257
Williams, J. P., & Myers, P. C. 1999, ApJ, 511, 208
Wouterloot, J. G. A., & Brand, J. 1989, A&AS, 80, 149
Wu, Y., Wei, Y., Zhao, M., et al. 2004, A&A, 426, 503
Zhang, Q., Hunter, T. R., Brand, J., et al. 2001, ApJ, 552, 167

---

[3] See footnote #2.